ACS APPLIED NANO MATERIALS

www.acsanm.org Article

Varying the Concentration of Organic Acid and Amine Ligands Allows Tuning between Quantum Dots and Magic-Sized Clusters of $CH_3NH_3PbBr_3$ Perovskite: Implications for Photonics and Energy Conversion

Li Liu, Ke Xu, Evan Thomas Vickers, A'Lester Allen, Xueming Li, Lijun Peng, and Jin Zhong Zhang*

Cite This: *ACS Appl. Nano Mater.* 2020, 3, 12379−12387 Read Online

ACCESS | Metrics & More | Article Recommendations | Supporting Information

ABSTRACT: Metal halide perovskites, such as methylammonium lead halide ($CH_3NH_3PbBr_3$), have recently attracted tremendous attention due to their outstanding properties and promising applications. Here, $CH_3NH_3PbBr_3$ perovskite magic-sized clusters (PMSCs) and perovskite quantum dots (PQDs) are synthesized by surface passivation with various organic acids and amines through a ligand-assisted reprecipitation process (LARP). Their optical properties are investigated with ultraviolet−visible (UV−vis) absorption and photoluminescence (PL) spectroscopy. The structures and optical properties of the PMSCs and PQDs can be controlled by varying the ligand/precursor ratio and type as well as the concentration of ligands. Specifically, a high ligand/precursor ratio and excessive amines favor PMSCs, whereas excessive acids lead to the generation of PQDs over PMSCs. As a result, we can tune between PQDs and PMSCs by changing the amine/acid ligand ratio. Energy-dispersive X-ray (EDS) elemental mapping confirms the presence of the constituent elements of the perovskite, namely, Pb and Br. With the help of Fourier transform infrared (FTIR) results, a model is proposed to explain the mechanism of formation of both PQDs and PMSCs as well as their interconversion in terms of the ligands passivating the surface defect sites. This study provides important insights into the fundamental growth mechanisms of perovskite nanostructures, especially in terms of the interplay between the perovskite precursors and passivating ligands. The work has significant implications in applications of metal halide perovskites in photonics and energy conversion.

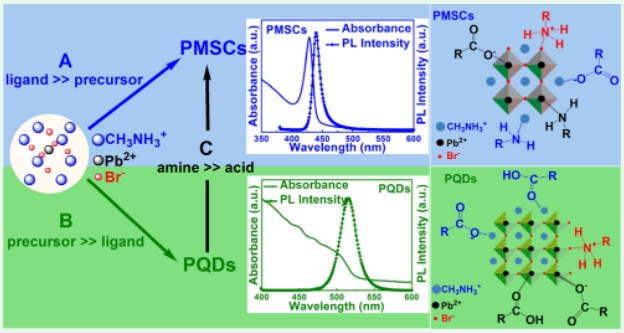

KEYWORDS: *methylammonium lead halide perovskites, quantum dots, magic-sized clusters, ligands, surface passivation*

INTRODUCTION

Perovskite quantum dots (PQDs) have received increasing interest due to their novel properties, such as high photoluminescence (PL) quantum efficiency and narrow but tunable emission bandwidth. The emission can be easily tuned over the entire visible spectrum by controlling the crystal size and halide ion composition, which are attractive for light-emitting diodes (LED),[1−4] solar cells,[5−9] and other optoelectronic applications.[1−5,7,10−13] Compared with perovskite bulk materials, PQDs exhibit tunable properties due to the quantum confinement effect and an extremely large surface-to-volume (S/V) ratio that allows for easy surface functionalization for different applications.[14−22] Compared with conventional PQDs, perovskite magic-sized clusters (PMSCs) with single size or narrow size distributions have narrower and bluer optical absorption bands and better-defined structures that are desired for fundamental studies.[23−26] For example, they are good model systems for understanding the growth of larger nanostructures including QDs or QD solids.[27−34]

Despite many advantages, there are two main challenges in the research of both PQDs and PMSCs. First, PQDs and PMSCs are unstable in high humidity and polar/protic solvents,[35,36] and there are many deficits in the understanding of their defect chemistry preventing their wide-scale application.[37−39] Due to the ionic nature of the perovskite core, there are many charging defects in perovskites, including positive-charge defects (i.e., a halide ion vacancy leading to undercoordinated Pb^{2+}), and negative-charge defects (i.e., a Cs^+, $CH_3NH_3^+$, or $CH(NH_2)_2^+$ cation vacancy and PbX_4^{2-} antisite defects).[40] This leads to perovskite degradation during storage or processing. After coming in contact with polar

Received: October 28, 2020
Accepted: December 1, 2020
Published: December 10, 2020

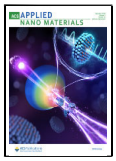

https://dx.doi.org/10.1021/acsanm.0c02894
ACS Appl. Nano Mater. 2020, 3, 12379−12387

media, such as alcohol and water, their colloidal properties decay and their absorption and emission features deteriorate.[41]

Both experimental and theoretical studies have shown that surface passivation can be used to effectively control defect activity in perovskites and improve their performance and stability.[42−44] Passivation treatment often results in a significant enhancement in PL and longer-lived excited charge-carrier lifetime in perovskites, which is usually interpreted as a decrease in nonradiative recombination centers.[40] Nenon et al. used the hard and soft acids and bases concept to develop a general ligand passivation scheme and showed that the tail group of carboxylates can be used to selectively coordinate or dissociate the ligands.[45] Several experimental studies have shown that the radiation recombination between charge traps is suppressed after the passivation, resulting in a blue shift in the PL peak.[23−26,46−52] Huang et al. performed a systematic study on how the amount of ligands (oleylamine and oleic acid), the precursor/ligand ratio, and the reaction temperature affect perovskites.[53] Tong et al. showed that the size of the perovskites decreased and the emission spectrum blue-shifted by controlling the degree of dilution.[54] These studies show that surface chemistry, such as the composition and concentration of capping ligands, have a significant impact on the optical properties of perovskites.[55−58]

Despite extensive studies of perovskite surface chemistry,[59] a detailed understanding of ligand−perovskite interaction is still lacking, especially in relation to PQDs and PMSCs. In our recent work, the optical properties, size, and stability of the PQDs and PMSCs are determined to be strongly ligand-dependent. By changing the amount of capping ligands used, we can easily tune PQDs to PMSCs or produce a mixture of the two.[23−25] Additionally, PQDs can be obtained in a series dilution of PMSCs in toluene.[26] Higher concentrations or stronger ligands favor PMSCs over PQDs because of the larger S/V ratio, and effective surface passivation requires more capping ligands. However, the possible effect of using different types of ligands on the synthesis of PQDs and PMSCs is currently unknown.

In this work, $CH_3NH_3PbBr_3$ PQDs and PMSCs were synthesized through a ligand-assisted reprecipitation process (LARP) with various organic acids and amines as capping ligands. We investigated the effects of the capping ligand concentration and the ligand/precursor ratio on the optical properties of the perovskite nanostructures. Interestingly, an excess of amine leads to the conversion of PQDs to PMSCs, while excess acid favors PQDs over PMSCs. Fourier transform infrared (FTIR) spectra have enabled us to identify a capping ligand shell surrounding the PQDs and PMSCs, thus enabling us to shed light on the possible passivation and transformation mechanisms. We demonstrated two possible individual pathways for the controllable synthesis of PMSCs and PQDs with tunable optical properties.

EXPERIMENTAL SECTION

Materials. Methylammonium bromide (CH_3NH_3Br, 99.9%, Greatcell Solar), $PbBr_2$ (99.999%, Alfa Aesar), *n*-octanoic acid (OcA, 98.0%, Tokyo Chemical Industry), oleic acid (OA, 90%, Sigma Aldrich), *n*-octylamine (OcAm, 98.0%, Tokyo Chemical Industry), butylamine (BTYA, 99%, Oakwood Chemical), *N*,*N*-dimethylformamide (DMF, 99.9%, Fisher Scientific), and toluene (99.9%, Fisher Scientific) were commercially available. All chemicals were used as received without any further purification.

Synthesis of $CH_3NH_3PbBr_3$ PQDs and PMSCs. In a typical synthesis process of $CH_3NH_3PbBr_3$ PQDs and PMSCs, CH_3NH_3Br (0.080 mmol, 9.0 mg), $PbBr_2$ (0.20 mmol, 73.0 mg), and 400 μL of DMF were added to a borosilicate vial and the solution was sonicated and heated until all solid dissolved. Next, OcA (1.0 mmol, 167 μL) was added to the solution and sonicated for 30 s. Then, OcAm (1.0 mmol, 160 μL) was added to the solution and sonicated for 30 s. One-hundred microliters of the precursor solution was injected at a fast rate to 5.0 mL of toluene under vigorous stirring. $CH_3NH_3PbBr_3$ perovskite samples were prepared by adding 50 μL of the as-synthesized solution into 5.0 mL of toluene.

Other syntheses reported in this study were carried out using similar reactions as above at a fixed precursor concentration and different concentrations of ligands. It was observed that the color of the solution changed from light yellow to yellow-green to clear and colorless as the ligand/precursor ratio increased, and the resulting solution remained clear for about 1.0 min before it gradually turned to a milky white suspension.

Spectroscopic Measurements. Ultraviolet-visible (UV−vis) absorption spectra were measured with an Agilent Technologies Cary 60 UV−vis spectrophotometer, and the PL spectra were measured using a HORIBA Jobin Yvon Fluoromax-3 spectrofluorometer using a quartz cuvette (1.0 cm × 1.0 cm) at room temperature. Scanning transmission electron microscopy (TEM) was performed by drop-casting particles on an EM grid (Electron Microscopy Sciences, CF-400-Cu) and acquiring scanning transmission electron microscopy with high-angle annular dark-field (STEM-HAADF) images with an FEI TitanX microscope operating at an acceleration voltage of 300 kV at the National Center for Electron Microscopy, Molecular Foundry, Lawrence Berkeley National Laboratory. The STEM probe had a convergence angle of 10 mrad and a beam current of ∼400 pA. Energy-dispersive X-ray spectroscopy (EDS) was performed using an FEI TitanX microscope operated at an acceleration voltage of 300 kV. FTIR spectra were obtained with a PerkinElmer FTIR spectrometer (Spectrum One, a spectral resolution of 4 cm^{-1}), where the samples were prepared by dropping the $CH_3NH_3PbBr_3$ solution onto a KBr pellet.

RESULTS AND DISCUSSION

Optical Properties of $CH_3NH_3PbBr_3$ PQDs and PMSCs. Here, we present results on the optical properties of the PQDs and PMSCs synthesized using surface ligands comprising OcA and OcAm. The PQDs and PMSCs consist of a $CH_3NH_3PbBr_3$ perovskite core passivated with a combination of OcA and OcAm as capping ligands, as illustrated in Scheme 1. While OcA and OcAm are first used in the synthesis, it is the proton transfer products that are more effective for passivation: carboxylate and ammonium ions.

Figure 1 shows the UV−vis electronic absorption and PL spectra of $CH_3NH_3PbBr_3$ PQDs and PMSCs with various ligand/precursor ratios. The molar ratio of OcA/OcAm was fixed at 1:1 with the concentration of OcA and OcAm varied as 0.025, 0.050, 0.25, 0.40, 0.50, and 1.0 mM, respectively. Three absorption bands were observed with peaks at 452, 474, and 510 nm for 0.025 mM OcA and OcAm. In the case with 0.050 mM OcA and OcAm, only one absorption peak at 438 nm was observed. With 0.25 mM OcA and OcAm, the absorption peak shifted to 430 nm and remained unchanged even after the ligand amount was further increased to 1.0 mM for both OcA and OcAm. According to previous studies, the range of 450−520 nm broader excitonic absorption peaks is attributed to PQDs,[60−62] while the single sharp excitonic absorption peak at around 430 nm is assigned to PMSCs.[23,25,26]

In the PL spectra, three PL emission peaks at 455, 475, and 513 nm were observed for 0.025 and 0.050 mM OcA and OcAm, while three PL emission peaks were observed at 436, 455, and 475 nm for 0.25 mM OcA and OcAm. Two PL emission peaks were observed at 436 and 455 nm for 0.40 mM

https://dx.doi.org/10.1021/acsanm.0c02894
ACS Appl. Nano Mater. 2020, 3, 12379−12387

Scheme 1. Illustration of PQDs or PMSCs Passivated with a Combination of OcA and OcAm Ligands

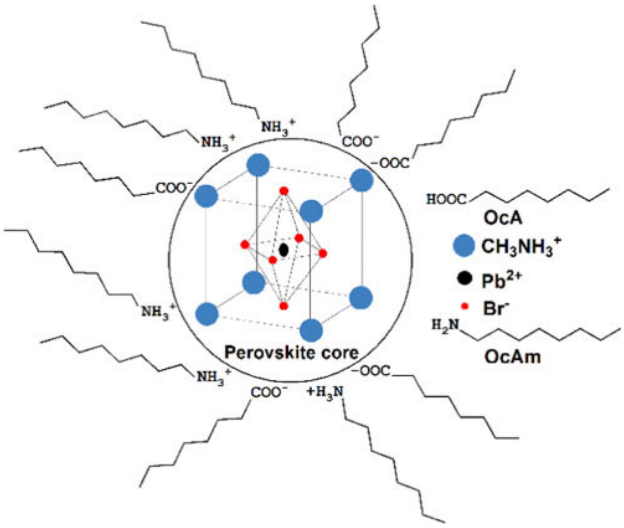

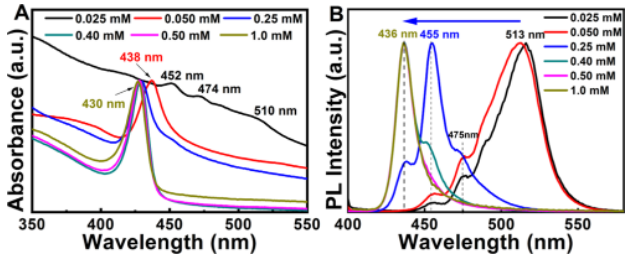

Figure 1. (A) UV−vis absorption and (B) PL spectra of $CH_3NH_3PbBr_3$ PQDs and PMSCs with various ligand/precursor ratios. The molar ratio of OcA/OcAm was fixed at 1:1, and the amounts of OcA and OcAm varied as 0.025, 0.050, 0.25, 0.40, 0.50, and 1.0 mM, respectively.

OcA and OcAm. With 0.50 and 1.0 mM OcA and OcAm, only one PL emission peak at 436 nm was observed. The PL emission peak at 513 nm corresponds to PQDs, while the strong and sharp excitonic emission peak at 436 nm is assigned to PMSCs, and the strong PL emission peak at 455 nm is not expected and may be due to the trap states of PMSCs.[26] The weak PL emission peak at 475 nm corresponds to smaller size PQDs. Details of the UV−vis absorption and PL emission peaks of $CH_3NH_3PbBr_3$ PQDs and PMSCs with various ligand/precursor ratios are summarized in the Supporting Information (Table S1).

Figure 2 shows the UV−vis absorption and PL spectra of $CH_3NH_3PbBr_3$ PQDs and PMSCs with different amounts of OcAm and OcA fixed at 0.50 mM. The absorption spectrum has multiple excitonic peaks at a low OcAm concentration (i.e., 0.050 mM). Upon increasing the OcAm concentration to 0.25 mM, the intensities of the longer wavelength absorption peaks decreased, while those at shorter wavelength increased. With further increasing OcAm to 0.50 mM, only the absorption peak around 431 nm is retained. This may indicate that PMSCs are being formed.[26] With 6.25 mM OcAm, an additional absorption peak was observed at 396 nm. Based on the previous study from our group, this peak can be attributed to molecular clusters (MCs).[26,63]

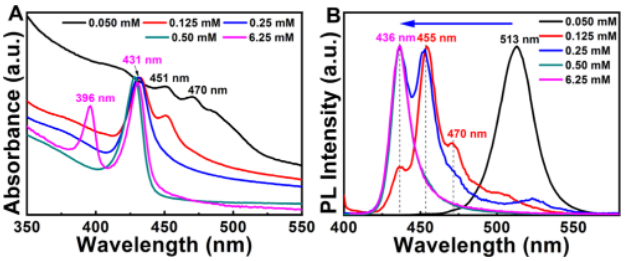

Figure 2. (A) UV−vis absorption and (B) PL spectra of OcA−OcAm $CH_3NH_3PbBr_3$ PQDs and PMSCs with different amounts of OcAm and OcA fixed at 0.50 mM. The amount of OcAm varied as 0.050, 0.125, 0.25, 0.50, and 6.25 mM, respectively.

A similar trend is observed in the PL spectra. Initially, for 0.050 mM OcAm, there was one broad emission peak at 513 nm, which was attributed to PQDs. As the concentration of OcAm increased (i.e., 0.125 mM), a new peak appeared at 455 nm, which was related to the trap state of PMSCs and accompanied by two shoulder peaks at 436 and 470 nm, attributing to PMSCs and smaller size PQDs formed, respectively. With further increasing OcAm concentration (i.e., 0.25 mM), the relative intensity of the blue shoulder peak at 436 nm continuously increased. A single PL emission peak at 436 nm was observed at high OcAm concentrations (i.e., 0.50 and 6.25 mM), indicative of pure PMSCs. Details of the UV−vis absorption and PL emission peaks of $CH_3NH_3PbBr_3$ PQDs and PMSCs with different amounts of OcAm are summarized in the Supporting Information (Table S2).

Figure 3 shows the evolution of the optical properties of the obtained $CH_3NH_3PbBr_3$ PQDs and PMSCs with different

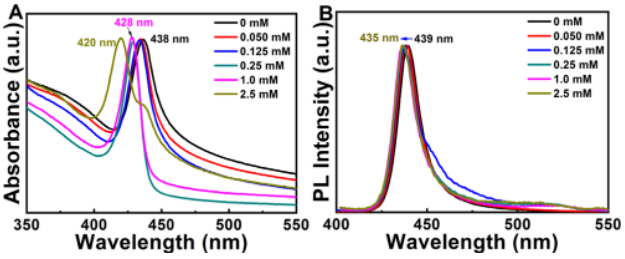

Figure 3. (A) UV−vis absorption and (B) PL spectra of OcA−OcAm $CH_3NH_3PbBr_3$ PQDs and PMSCs with different amounts of OcA and OcAm fixed at 0.50 mM. The amount of OcA varied as 0, 0.050, 0.125, 0.25, 1.0, and 2.5 mM, respectively.

concentrations of OcA with OcAm fixed at 0.50 mM. Interestingly, when adding only OcA as a capping ligand, the perovskite solution showed an exciton absorption peak at 438 nm and a PL peak at 439 nm, which is attributed to PMSCs. With the addition of OcA to 2.5 mM, the absorption maximum blue-shifted to 420 nm, while the PL peak blue-shifted from 439 to 435 nm. The blue shift could be explained by the strong quantum confinement effect due to the formation of extremely small size PMSCs relative to the exciton Bohr radius.[21] Details of the UV−vis absorption and PL emission peaks of $CH_3NH_3PbBr_3$ PQDs and PMSCs with different amounts of OcA are summarized in the Supporting Information (Table S3).

As the ligand/precursor ratio and OcAm concentration increases, the first absorption peak blue-shifts from 510 to 430 nm while the first PL peak blue-shifts from 513 to 436 nm. In

https://dx.doi.org/10.1021/acsanm.0c02894
ACS Appl. Nano Mater. 2020, 3, 12379−12387

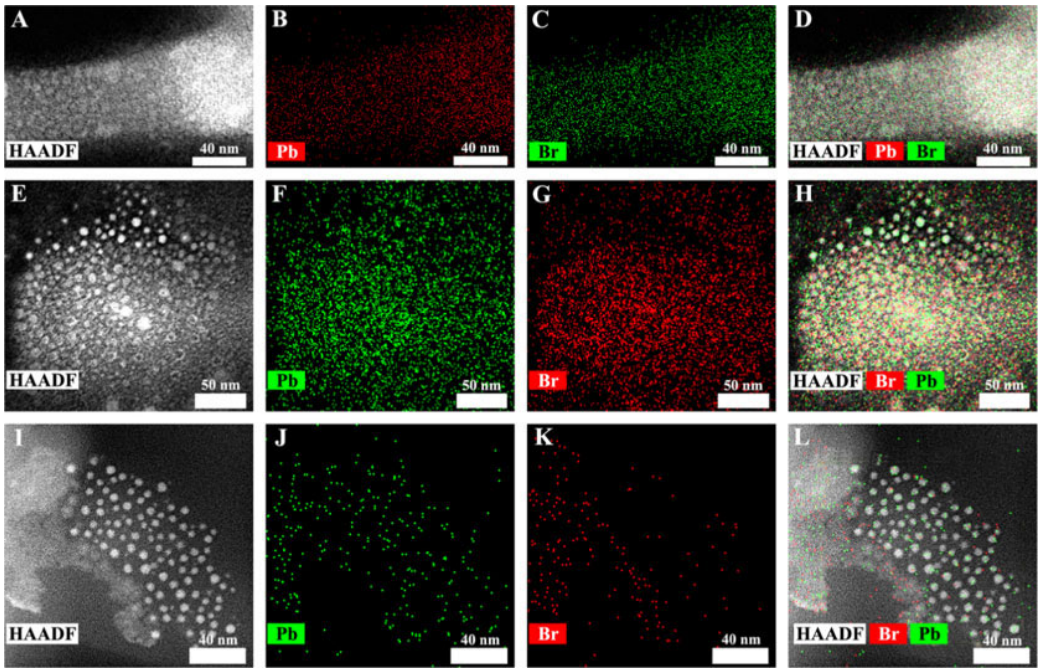

Figure 4. (A) STEM-HAADF image of OcAm PMSCs, (B–D) EDS elemental mapping of Pb (red), Br (green), and composite map (scale bar, 40 nm), (E) STEM-HAADF image of OA–OcAm PMSCs, (F–H) EDS elemental mapping of Pb (green), Br (red), and composite map (scale bar, 50 nm), (I) STEM-HAADF image of OA–OcAm PQDs, and (J–L) EDS elemental mapping of Pb (green), Br (red), and composite map (scale bar, 40 nm).

addition, the multiple absorption and PL bands at longer wavelengths disappeared. However, as the OcA concentration increases, slight blue shifts from 438 to 420 and 439 to 435 nm are found in the absorption and emission bands, respectively. These results suggest that the high ligand/precursor ratio and excessive OcAm favor $CH_3NH_3PbBr_3$ PMSCs over PQDs. To better understand the intricate effect of different amine and acid ligands on the formation of $CH_3NH_3PbBr_3$ PQDs and PMSCs, a series of control experiments with ligand variations were conducted by replacing OcAm with BTYA and OcA with OA under otherwise identical conditions.

UV–vis absorption and PL spectra of OcA–BTYA and OA–OcAm $CH_3NH_3PbBr_3$ PQDs and PMSCs with different amounts of amine while the amount of the acid was fixed at 0.50 mM are shown in the Supporting Information (Figure S1). For OcA–BTYA $CH_3NH_3PbBr_3$ PQDs and PMSCs, five absorption bands were observed with peaks at 405, 438, 454, 471, and 508 nm with 0.050 mM BTYA. The 405 nm absorption peak is attributed to MCs,[63] the 438 nm peak is attributed to PMSCs, the 454 nm peak is due to the trap state of PMSCs, and the 471 and 508 nm peaks are attributed to PQDs of different sizes. Only one absorption peak at 438 and 405 nm was observed with 0.25 and 1.5 mM BTYA, respectively. For OA–OcAm $CH_3NH_3PbBr_3$ PQDs and PMSCs, three absorption bands were observed with peaks at 450, 470, and 508 nm with 0.050 mM OcAm. Only one absorption peak at 426 nm was observed with 0.125 and 0.25 mM OcAm. With 1.0 mM OcAm, the absorption peak shifted to 396 nm.

A strong PL emission peak at 518 nm was observed with 0.05 mM BTYA for OcA–BTYA $CH_3NH_3PbBr_3$ PQDs and PMSCs. Interestingly, three PL emission peaks at 455, 475, and 500 nm were observed with 0.125 and 0.25 mM BTYA, while only one sharp excitonic absorption peak is observed in the corresponding absorption spectra. This could be due to different sized PQDs forming in solution. With 1.5 mM BTYA, only one PL emission peak at 436 nm was observed, indicating pure PMSCs. For OA–OcAm $CH_3NH_3PbBr_3$ PQDs and PMSCs, a strong PL emission peak at 513 nm was observed with 0.05 mM OcAm. As the amount of OcAm increases, the PL emission peak blue-shifts to 436 nm. Details of the UV–vis absorption and PL emission peaks of $CH_3NH_3PbBr_3$ PQDs and PMSCs with different amounts of amine are summarized in the Supporting Information (Table S2).

UV–vis absorption and PL spectra of OcA–BTYA and OA–OcAm $CH_3NH_3PbBr_3$ PQDs and PMSCs with different concentrations of the acid as a capping ligand while the concentration of amine was fixed at 0.50 mM are shown in the Supporting Information (Figure S2). When OcAm was replaced with BTYA, two absorption peaks were observed at 407 and 440 nm, corresponding to MCs and PMSCs, respectively. With the addition of OcA, the absorption peak at 404 nm gradually disappeared. When the amount of OcA increased to 2.5 mM, only one absorption peak at 431 nm was observed. When OcA was replaced with OA by retaining OcAm, the absorption peak blue-shifted to 420 nm as the amount of OA increased.

Meanwhile, for the OcA–BTYA $CH_3NH_3PbBr_3$ sample, initially, there were two excitonic emission peaks at 410 and 440 nm, which were attributed to MCs and PMSCs, respectively. With the addition of OcA, a new emission peak appeared at 488 nm, which was attributed to PQDs, and then blue-shifted to 455 nm, which was the trap state of PMSCs. With the addition of OcA to 2.5 mM, there was only one emission peak at 440 nm, accompanied by the disappearance of multiple PL bands, indicative of pure PMSCs. For OA–OcAm $CH_3NH_3PbBr_3$ PQDs and PMSCs, although the addition of OA did not affect the main emission peak at 436

https://dx.doi.org/10.1021/acsanm.0c02894
ACS Appl. Nano Mater. 2020, 3, 12379–12387

nm, several weak emission bands appeared at 452, 470, and 513 nm. However, for high concentration OA samples (i.e., 1.0 and 2.5 mM), the three weak emission peaks disappeared. This may be caused by the formation of PQDs, but the large excess of amine would have the ability to render them down into PMSCs. Details of the UV−vis absorption and PL emission peaks of $CH_3NH_3PbBr_3$ PQDs and PMSCs with different amounts of the acid are summarized in the Supporting Information (Table S3).

As the amount of amine increased, the absorption and emission characteristics of both OcA−BTYA and OA−OcAm samples showed a continuous blue shift. However, as the concentration of the acid increased, the absorption showed a minor blue shift from 438 to 420 nm and the PL emission peak around 436 nm gradually increased. This is similar to the case of OcA−OcAm samples, which reveals that it would be possible to obtain pure PMSCs with only one peak at a fixed wavelength in the PL spectra by controlling the ligand concentration. These results clearly point to the pivotal role that amine plays in the formation of PMSCs.

Structural Properties of $CH_3NH_3PbBr_3$ PQDs and PMSCs. Figure 4 shows STEM-HAADF images of representative samples of OcAm PMSCs, OA−OcAm PMSCs, and OA−OcAm PQDs. The average particle sizes for the samples of OcAm PMSCs, OA−OcAm PMSCs, and OA−OcAm PQDs are 4.1 ± 0.9, 4.9 ± 1.7, and 5.0 ± 0.9 nm, respectively. High-resolution TEM (HRTEM) and size distribution histograms are provided in the Supporting Information (Figure S3). The PMSCs are larger than estimated based on the previous literature.[24,26] This may be due to further growth or aggregation of the PMSCs into a larger structure during the preparation of the EM grid. In the process of making the EM grid, the toluene solvent evaporates to produce a supersaturated solution, which may make the PMSCs grow or aggregate into a larger structure during the drying process. A combination of HAADF with EDS elemental mapping confirms the presence of the constituent elements of the perovskite, namely, Pb and Br (Figure 4B,C,F,G,J,K). The relative ratio of the Pb/Br ratio of PMSCs and PQDs was also determined by applying EDS measurements (see Table S4 in the Supporting Information).

FTIR spectra were measured to understand the state of the surface ligands in $CH_3NH_3PbBr_3$ PQDs and PMSCs. As shown in Figure 5, for OcAm PMSCs, the characteristic bands at 2855 and 2923 cm^{-1} are assigned to symmetric and asymmetric CH_2 stretching modes,[61,64] and the band at 1465 cm^{-1} can be assigned to CH_2 bending vibration. The NH_2 bending at around 1600 cm^{-1} shifts to 1577 cm^{-1} upon coordination to metals, indicating the presence of OcAm on the PMSC surface. For OA−OcAm PMSCs, the bands at 1450 and 1580 cm^{-1} are corresponding to the symmetric and asymmetric stretching vibrations of the COO^- group, respectively.[65] The bands at 1493 and 1602 cm^{-1} are attributed to the symmetric and asymmetric deformation vibrations of the NH_3^+ group, respectively.[66] A relatively broad band in the 1530−1600 cm^{-1} range emerges in OcA−OcAm PMSC FTIR spectrum, which can be attributed to the superposition of the COO^- asymmetric stretching vibration and NH_3^+ symmetric and asymmetric deformation vibrations.[67] For OA−OcAm PQDs and OcA−OcAm PQDs, the characteristic peaks at 1410 and 1711 cm^{-1} are attributed to the asymmetric and symmetric vibrations of C═O and C−O in the carboxylic acid form.[26,64] The FTIR results indicate that the surface of PMSCs primarily has amine, NH_3^+, and COO^-, while PQDs have the acid, COO^-, and NH_3^+. The detailed FTIR results are summarized in the Supporting Information (Table S5).

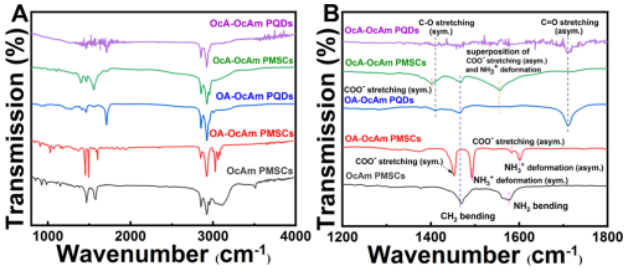

Figure 5. FTIR spectra of OcAm PMSCs, OA−OcAm PMSCs, OA−OcAm PQDs, OcA−OcAm PMSCs, and OcA−OcAm PQDs: (A) overall peak shape and (B) 1200−1800 cm^{-1} range.

PMSCs are formed only when the concentration of amine is high. To help understand the reason behind, we calculated the reaction equilibrium constants (K_{eq}) for OcA with OcAm and OA with OcAm. The K_{eq} values of OcA/OcAm and OA/OcAm are calculated to be 7.58×10^5 and 5.62×10^5, respectively (details are given in the Supporting Information). OcA and OA can transfer protons to OcAm, generating ammonium cations (NH_3^+). High amine concentration leads to more NH_3^+, which can effectively passivate Br^- defects.

For OcAm PMSCs without acid ligands, while OcAm can passivate surface Pb^{2+} or $CH_3NH_3^+$ defects using lone pair electrons on the N atom, there is no cationic ligand available to passivate the Br^- defects, resulting in poor stability as observed.

In contrast, we found that high acid ligand concentration favors PQDs over PMSCs. In this case, amine deprotonates carboxylic acid into a carboxylate anion (COO^-), which should be effective in passivating Pb^{2+} and $CH_3NH_3^+$ defects. Based on this, we suggest that the PMSC surface is mainly passivated by amine and NH_3^+ ligands, while the PQD surface is primarily passivated by the acid (using lone pair electrons on O) and COO^-. This suggestion is supported by the FTIR results.

Mechanism of Ligand-Promoted Perovskite Formation. Figure 6 illustrates the proposed growth mechanisms for $CH_3NH_3PbBr_3$ PQDs and PMSCs, and the dependence of their conversion on the amount and ratio of ligands. At low ligand concentrations, only PQDs form, while PMSCs cannot form, since they require better passivation than PQDs due to smaller size and a larger S/V ratio, which can be achieved via either a high concentration of ligands or strong ligands.[23−26] Once the ligand concentration increases, the probability of forming PMSCs increases, as excessive ligands can provide the passivation needed by the PMSCs.

At least three types of surface defect sites are expected for $CH_3NH_3PbBr_3$ perovskites due to the three components: $CH_3NH_3^+$, Pb^{2+}, and Br^-.[68,69] In the case of $CH_3NH_3PbBr_3$ PQDs, the acid and amine ligands are used in conjunction, and the proton transfer reaction between them leads to R−COO^- that binds to $CH_3NH_3^+$ or Pb^{2+} and to R′−NH_3^+ (R or R′ = alkyl chain) that binds to Br^-. The protonation reaction between amine and acid ligands can be described by eq 1

$$R - COOH + R' - NH_2 \leftrightarrow R - COO^- + R' - NH_3^+ \quad (1)$$

https://dx.doi.org/10.1021/acsanm.0c02894
ACS Appl. Nano Mater. 2020, 3, 12379−12387

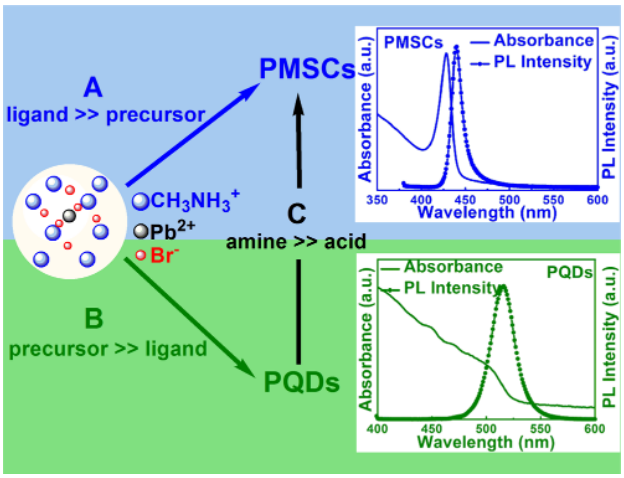

Figure 6. Schematic illustration of the growth mechanism of $CH_3NH_3PbBr_3$ PQDs and PMSCs, and dependence of their conversion on the amount and ratio of ligands.

Considering that the acid was mixed with amine with a higher molar ratio (10:1), the excess carboxylic acid can also passivate cationic defect sites with the lone pair electrons in the oxygen atoms in the −COOH group, which is likely less effective compared to the ionic ligands generated following eq 1.

In the case of $CH_3NH_3PbBr_3$ PMSCs, the general strategy of passivation is very similar to that of PQDs. The main difference is that PMSCs are smaller than PQDs and have a larger S/V ratio and therefore require better protection with ligands. Based on eq 1, a high concentration of the acid or amine ligand helps to push the reaction to the right-hand side and produce more $R{-}COO^-$ and $R'{-}NH_3^+$, which are expected to passivate perovskite surface defects more effectively, thus leading to the formation of PMSCs.

Interestingly, $CH_3NH_3PbBr_3$ PMSCs can also be obtained by adding only a high concentration of amine as a ligand. This is possibly because amine is a strong ligand for passivating surface defects. The amine ligand can directly bind to Pb^{2+} or $CH_3NH_3^+$ because it can readily donate lone pair electrons on the nitrogen atom to Pb^{2+} or $CH_3NH_3^+$ to form a Pb^{2+}−amine or $CH_3NH_3^+$−amine bond. When the acid is added and the amine is converted into ammonium, the $R'{-}NH_3^+$ and $R{-}COO^-$ produced via eq 1 can now passivate respective anionic (Br^-) and cationic (Pb^{2+} and $CH_3NH_3^+$) charged surface defects, similar to what happens for PQDs.

The surface passivation mechanism of $CH_3NH_3PbBr_3$ PQDs and PMSCs is illustrated in Figure 7. In general, excess ligands

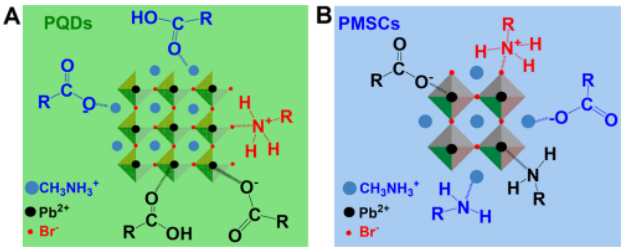

Figure 7. Schematic diagram illustrating the surface passivation mechanism of (A) $CH_3NH_3PbBr_3$ PQDs and (B) PMSCs surface defects.

are essential for efficient passivation and therefore for the generation of PMSCs that are smaller in size and have larger S/V ratios than PQDs, thus requiring better passivation than PQDs. As the concentration of ligands increases, especially amine ligands, the passivation becomes more effective and PMSCs become more dominant over PQDs. Excessive amine can thus lead to the conversion of PQDs to PMSCs.

CONCLUSIONS

In summary, $CH_3NH_3PbBr_3$ PQDs and PMSCs were synthesized using two different acid capping ligands, OcA and OA, and two different amine ligands, OcAm and BTYA. The effects of the ligand/precursor ratio and the concentration of ligands on the optical properties of PMSCs and PQDs were investigated. For all of the samples, a conversion from PQDs to PMSCs was observed, with a high ligand/precursor ratio and excessive amines favoring $CH_3NH_3PbBr_3$ PMSCs over PQDs. We suggest that with an increase in the concentration of ligands, especially amine ligands, the passivation becomes more effective and PMSCs become more dominant over PQDs due to effective chemical passivation of the surface. FTIR analysis further elucidated the surface ligand composition and the underlying coverage mechanism. This study helps to gain deeper insights into the controllable synthesis and growth mechanism of $CH_3NH_3PbBr_3$ PMSCs and PQDs with tunable electronic and optical properties. This has important implications in applications of perovskite materials in the fields of photonics and energy conversion, including solar cells, LEDs, and sensing. The strategy developed in using the amine/acid ratio to control the relative amount of PMSCs and PQDs produced should be general and can be easily extended to other amines and acids for such purposes.

ASSOCIATED CONTENT

Supporting Information

The Supporting Information is available free of charge at https://pubs.acs.org/doi/10.1021/acsanm.0c02894.

UV−vis and PL spectra as well as HRTEM images of PQDs and PMSCs; tabulation of peaks and assignments of UV−vis, PL, and IR spectra; and summary of dissociation constants and equilibrium constants of OcA/OcAm and OA/OcAm ligands (PDF)

AUTHOR INFORMATION

Corresponding Author

Jin Zhong Zhang − *Department of Chemistry and Biochemistry, University of California, Santa Cruz, California 95064, United States;* orcid.org/0000-0003-3437-912X; Email: zhang@ucsc.edu

Authors

Li Liu − *Research Institute of Agricultural Quality Standards and Testing Technology, Hubei Academy of Agricultural Science, Wuhan 430064, P. R. China; Department of Chemistry and Biochemistry, University of California, Santa Cruz, California 95064, United States*

Ke Xu − *Department of Chemistry and Biochemistry, University of California, Santa Cruz, California 95064, United States; College of Chemistry and Chemical Engineering, Chongqing University, Chongqing 401331, P. R. China*

https://dx.doi.org/10.1021/acsanm.0c02894
ACS Appl. Nano Mater. 2020, 3, 12379−12387

Evan Thomas Vickers − *Department of Chemistry and Biochemistry, University of California, Santa Cruz, California 95064, United States;* orcid.org/0000-0002-9594-4279

A'Lester Allen − *Department of Chemistry and Biochemistry, University of California, Santa Cruz, California 95064, United States*

Xueming Li − *College of Chemistry and Chemical Engineering, Chongqing University, Chongqing 401331, P. R. China*

Lijun Peng − *Research Institute of Agricultural Quality Standards and Testing Technology, Hubei Academy of Agricultural Science, Wuhan 430064, P. R. China*

Complete contact information is available at: https://pubs.acs.org/10.1021/acsanm.0c02894

Author Contributions

All authors have approved the final version of the manuscript.

Notes

The authors declare no competing financial interest.

■ ACKNOWLEDGMENTS

This work is supported by the NSF (CHE-1904547). Work at the Molecular Foundry was supported by the Office of Science, Office of Basic Energy Sciences, of the U.S. Department of Energy under Contract No. DE-AC02-05CH11231. L.L. is grateful for support from the Hubei Academy of Agricultural Science Visiting Scholar Program (Grant No. Q2018034).

■ REFERENCES

(1) Liu, R.; Xu, K. Blue perovskite light-emitting diodes (LEDs): A minireview. *Instrum. Sci. Technol.* **2020**, *48*, 616−636.

(2) Dong, Y.; Wang, Y. K.; Yuan, F.; Johnston, A.; Liu, Y.; Ma, D.; Choi, M. J.; Chen, B.; Chekini, M.; Baek, S. W.; Sagar, L. K.; Fan, J.; Hou, Y.; Wu, M.; Lee, S.; Sun, B.; Hoogland, S.; Quintero-Bermudez, R.; Ebe, H.; Todorovic, P.; Dinic, F.; Li, P.; Kung, H. T.; Saidaminov, M. I.; Kumacheva, E.; Spiecker, E.; Liao, L. S.; Voznyy, O.; Lu, Z. H.; Sargent, E. H. Bipolar-shell Resurfacing for Blue LEDs Based on Strongly Confined Perovskite Quantum Dots. *Nat. Nanotechnol.* **2020**, *15*, 668−674.

(3) Li, Z.; Song, C.; Li, J.; Liang, G.; Rao, L.; Yu, S.; Ding, X.; Tang, Y.; Yu, B.; Ou, J.; Lemmer, U.; Gomard, G. Highly Efficient and Water-Stable Lead Halide Perovskite Quantum Dots Using Super-hydrophobic Aerogel Inorganic Matrix for White Light-Emitting Diodes. *Adv. Mater. Technol.* **2020**, *5*, No. 1900941.

(4) Park, Y. J.; Kim, M.; Song, A.; Kim, J. Y.; Chung, K. B.; Walker, B.; Seo, J. H.; Wang, D. H. Light-Emitting Transistors with High Color Purity Using Perovskite Quantum Dot Emitters. *ACS Appl. Mater. Interfaces* **2020**, *12*, 35175−35180.

(5) Kim, J. Y.; Lee, J. W.; Jung, H. S.; Shin, H.; Park, N. G. High-Efficiency Perovskite Solar Cells. *Chem. Rev.* **2020**, *120*, 7867−7918.

(6) Jia, D.; Chen, J.; Yu, M.; Liu, J.; Johansson, E. M. J.; Hagfeldt, A.; Zhang, X. Dual Passivation of $CsPbI_3$ Perovskite Nanocrystals with Amino Acid Ligands for Efficient Quantum Dot Solar Cells. *Small* **2020**, *16*, No. 2001772.

(7) Li, Y.; Zhang, X.; Huang, H.; Kershaw, S. V.; Rogach, A. L. Advances in Metal Halide Perovskite Nanocrystals: Synthetic Strategies, Growth Mechanisms, and Optoelectronic Applications. *Mater. Today* **2020**, *32*, 204−221.

(8) Tan, H.; Jain, A. J.; Voznyy, O.; Lan, X. Z.; De Arquer, F. P. G.; Fan, J. Z.; Quintero-Bermudez, R.; Yuan, M. J.; Zhang, B.; Zhao, Y. C.; Fan, F. J.; Li, P. C.; Quan, L. N.; Zhao, Y. B.; Lu, Z. H.; Yang, Z. Y.; Hoogland, S.; Sargent, E. H. Efficient and Stable Solution-Processed Planar Perovskite Solar Cells via Contact Passivation. *Science* **2017**, *355*, 722−726.

(9) Wang, Y. B.; Wu, T. H.; Barbaud, J.; Kong, W. Y.; Cui, D. Y.; Chen, H.; Yang, X. D.; Han, L. Y. Stabilizing Heterostructures of Soft Perovskite Semiconductors. *Science* **2019**, *365*, 687−691.

(10) Bera, S.; Pradhan, N. Perovskite Nanocrystal Heterostructures: Synthesis, Optical Properties, and Applications. *ACS Energy Lett.* **2020**, *5*, 2858−2872.

(11) Fu, P.; Shan, Q.; Shang, Y.; Song, J.; Zeng, H.; Ning, Z.; Gong, J. Perovskite Nanocrystals: Synthesis, Properties and Applications. *Sci. Bull.* **2017**, *62*, 369−380.

(12) Mitzi, D. B. Introduction: Perovskites. *Chem. Rev.* **2019**, *119*, 3033−3035.

(13) Long, G.; Sabatini, R.; Saidaminov, M. I.; Lakhwani, G.; Rasmita, A.; Liu, X.; Sargent, E. H.; Gao, W. Chiral-perovskite Optoelectronics. *Nat. Rev. Mater.* **2020**, *5*, 423−439.

(14) Li, G.; Huang, J.; Zhu, H.; Li, Y.; Tang, J.-X.; Jiang, Y. Surface Ligand Engineering for Near-Unity Quantum Yield Inorganic Halide Perovskite QDs and High-Performance QLEDs. *Chem. Mater.* **2018**, *30*, 6099−6107.

(15) Delmas, W. G.; Vickers, E. T.; DiBenedetto, A. C.; Lum, C.; Hernandez, I. N.; Zhang, J. Z.; Ghosh, S. Modulating Charge Carrier Dynamics and Transfer via Surface Modifications in Organometallic Halide Perovskite Quantum Dots. *J. Phys. Chem. Lett.* **2020**, *11*, 7886−7892.

(16) Park, J. H.; Lee, A. Y.; Yu, J. C.; Nam, Y. S.; Choi, Y.; Park, J.; Song, M. H. Surface Ligand Engineering for Efficient Perovskite Nanocrystal-Based Light-Emitting Diodes. *ACS Appl. Mater. Interfaces* **2019**, *11*, 8428−8435.

(17) Wang, T.; Wei, X.; Zong, Y.; Zhang, S.; Guan, W. An Efficient and Stable Fluorescent Sensor Based on APTES-functionalized $CsPbBr_3$ Perovskite Quantum Dots for Ultrasensitive Tetracycline Detection in Ethanol. *J. Mater. Chem. C* **2020**, *8*, 12196−12203.

(18) Yang, W.; Su, R.; Luo, D.; Hu, Q.; Zhang, F.; Xu, Z.; Wang, Z.; Tang, J.; Lv, Z.; Yang, X.; Tu, Y.; Zhang, W.; Zhong, H.; Gong, Q.; Russell, T. P.; Zhu, R. Surface Modification Induced by Perovskite Quantum Dots for Triple-cation Perovskite Solar Cells. *Nano Energy* **2020**, *67*, No. 104189.

(19) Ijaz, P.; Imran, M.; Soares, M. M.; Tolentino, H. C. N.; Martin-Garcia, B.; Giannini, C.; Moreels, I.; Manna, L.; Krahne, R. Composition-, Size-, and Surface Functionalization-Dependent Optical Properties of Lead Bromide Perovskite Nanocrystals. *J. Phys. Chem. Lett.* **2020**, *11*, 2079−2085.

(20) DuBose, J. T.; Kamat, P. V. Surface Chemistry Matters. How Ligands Influence Excited State Interactions between $CsPbBr_3$ and Methyl Viologen. *J. Phys. Chem. C* **2020**, *124*, 12990−12998.

(21) R, S.; Vishaka, H. V.; J, K.; Balakrishna, R. G. Green to Blue Light Emitting $CsPbBr_3$ Perovskite by Ligand Exchange and its Encapsulation by TiO_2 for Tandem Effect in Photovoltaic Applications. *ACS Appl. Nano Mater.* **2020**, *3*, 6089−6098.

(22) Jancik Prochazkova, A.; Demchyshyn, S.; Yumusak, C.; Másilko, J.; Brüggemann, O.; Weiter, M.; Kaltenbrunner, M.; Sariciftci, N. S.; Krajcovic, J.; Salinas, Y.; Kovalenko, A. Proteinogenic Amino Acid Assisted Preparation of Highly Luminescent Hybrid Perovskite Nanoparticles. *ACS Appl. Nano Mater.* **2019**, *2*, 4267−4274.

(23) Xu, K.; Vickers, E. T.; Luo, B.; Wang, Q.; Allen, A. L. C.; Wang, H.; Cherrette, V.; Li, X.; Zhang, J. Z. Room Temperature Synthesis of Cesium Lead Bromide Perovskite Magic Sized Clusters with Controlled Ratio of Carboxylic Acid and Benzylamine Capping Ligands. *Sol. Energy Mater. Sol. Cells* **2020**, *208*, No. 110341.

(24) Xu, K.; Vickers, E. T.; Luo, B.; Allen, A. C.; Chen, E.; Roseman, G.; Wang, Q.; Kliger, D. S.; Millhauser, G. L.; Yang, W.; Li, X.; Zhang, J. Z. First Synthesis of Mn-Doped Cesium Lead Bromide Perovskite Magic Sized Clusters at Room Temperature. *J. Phys. Chem. Lett.* **2020**, *11*, 1162−1169.

(25) Xu, K.; Allen, A. C.; Luo, B.; Vickers, E. T.; Wang, Q.; Hollingsworth, W. R.; Ayzner, A. L.; Li, X.; Zhang, J. Z. Tuning from Quantum Dots to Magic Sized Clusters of $CsPbBr_3$ Using Novel Planar Ligands Based on the Trivalent Nitrate Coordination Complex. *J. Phys. Chem. Lett.* **2019**, *10*, 4409−4416.

(26) Vickers, E. T.; Xu, K.; Dreskin, B. W.; Graham, T. A.; Li, X.; Zhang, J. Z. Ligand Dependent Growth and Optical Properties of Hybrid Organo-metal Halide Perovskite Magic Sized Clusters. *J. Phys. Chem. C* **2019**, *123*, 18746−18752.
(27) Chen, M.; Luan, C.; Zhang, M.; Rowell, N.; Willis, M.; Zhang, C.; Wang, S.; Zhu, X.; Fan, H.; Huang, W.; Yu, K.; Liang, B. Evolution of CdTe Magic-Size Clusters with Single Absorption Doublet Assisted by Adding Small Molecules during Prenucleation. *J. Phys. Chem. Lett.* **2020**, *11*, 2230−2240.
(28) Dmitruk, I.; Belosludov, R. V.; Dmytruk, A.; Noda, Y.; Barnakov, Y.; Park, Y. S.; Kasuya, A. Experimental and Computational Studies of the Structure of CdSe Magic-Size Clusters. *J. Phys. Chem. A* **2020**, *124*, 3398−3406.
(29) Gao, D.; Hao, X.; Rowell, N.; Kreouzis, T.; Lockwood, D. J.; Han, S.; Fan, H.; Zhang, H.; Zhang, C.; Jiang, Y.; Zeng, J.; Zhang, M.; Yu, K. Formation of Colloidal Alloy Semiconductor CdTeSe Magic-size Clusters at Room Temperature. *Nat. Commun.* **2019**, *10*, No. 1674.
(30) Luan, C.; Tang, J.; Rowell, N.; Zhang, M.; Huang, W.; Fan, H.; Yu, K. Four Types of CdTe Magic-Size Clusters from One Prenucleation Stage Sample at Room Temperature. *J. Phys. Chem. Lett.* **2019**, *10*, 4345−4353.
(31) Kastilani, R.; Bishop, B. P.; Holmberg, V. C.; Pozzo, L. D. On-Demand Sonochemical Synthesis of Ultrasmall and Magic-Size CdSe Quantum Dots in Single-Phase and Emulsion Systems. *Langmuir* **2019**, *35*, 16583−16592.
(32) Cunningham, P. D.; Coropceanu, I.; Mulloy, K.; Cho, W.; Talapin, D. V. Quantized Reaction Pathways for Solution Synthesis of Colloidal ZnSe Nanostructures: A Connection between Clusters, Nanowires, and Two-Dimensional Nanoplatelets. *ACS Nano* **2020**, *14*, 3847−3857.
(33) Zhang, J.; Hao, X.; Rowell, N.; Kreouzis, T.; Han, S.; Fan, H.; Zhang, C.; Hu, C.; Zhang, M.; Yu, K. Individual Pathways in the Formation of Magic-Size Clusters and Conventional Quantum Dots. *J. Phys. Chem. Lett.* **2018**, *9*, 3660−3666.
(34) Palencia, C.; Yu, K.; Boldt, K. The Future of Colloidal Semiconductor Magic-Size Clusters. *ACS Nano* **2020**, *14*, 1227−1235.
(35) Saidaminov, M. I.; Kim, J.; Jain, A.; Quintero-Bermudez, R.; Tan, H.; Long, G.; Tan, F.; Johnston, A.; Zhao, Y.; Voznyy, O.; Sargent, E. H. Suppression of Atomic Vacancies via Incorporation of Isovalent Small Ions to Increase the Stability of Halide Perovskite Solar Cells in Ambient Air. *Nat. Energy* **2018**, *3*, 648−654.
(36) Yang, S.; Chen, S. S.; Mosconi, E.; Fang, Y. J.; Xiao, X.; Wang, C. C.; Zhou, Y.; Yu, Z. H.; Zhao, J. J.; Gao, Y. L.; De Angelis, F.; Huang, J. S. Stabilizing Halide Perovskite Surfaces for Solar Cell Operation with Wide-bandgap Lead Oxysalts. *Science* **2019**, *365*, 473−478.
(37) Li, W.; Lai, X.; Meng, F.; Li, G.; Wang, K.; Kyaw, A. K. K.; Sun, X. W. Efficient Defect-passivation and Charge-transfer with Interfacial Organophosphorus Ligand Modification for Enhanced Performance of Perovskite Solar Cells. *Sol. Energy Mater. Sol. Cells* **2020**, *211*, No. 110527.
(38) González-Pedro, V.; Veldhuis, S. A.; Begum, R.; Bañuls, M. J.; Bruno, A.; Mathews, N.; Mhaisalkar, S.; Maquieira, Á. Recovery of Shallow Charge-Trapping Defects in $CsPbX_3$ Nanocrystals through Specific Binding and Encapsulation with Amino-Functionalized Silanes. *ACS Energy Lett.* **2018**, *3*, 1409−1414.
(39) Liu, Y.; Palotas, K.; Yuan, X.; Hou, T.; Lin, H.; Li, Y.; Lee, S. T. Atomistic Origins of Surface Defects in $CH_3NH_3PbBr_3$ Perovskite and Their Electronic Structures. *ACS Nano* **2017**, *11*, 2060−2065.
(40) Ono, L. K.; Liu, S. Z.; Qi, Y. B. Reducing Detrimental Defects for High-Performance Metal Halide Perovskite Solar Cells. *Angew. Chem., Int. Ed.* **2020**, *59*, 6676−6698.
(41) Wang, S.; Du, L.; Jin, Z.; Xin, Y.; Mattoussi, H. Enhanced Stabilization and Easy Phase Transfer of $CsPbBr_3$ Perovskite Quantum Dots Promoted by High-Affinity Polyzwitterionic Ligands. *J. Am. Chem. Soc.* **2020**, *142*, 12669−12680.
(42) Motti, S. G.; Meggiolaro, D.; Martani, S.; Sorrentino, R.; Barker, A. J.; De Angelis, F.; Petrozza, A. Defect Activity in Lead Halide Perovskites. *Adv. Mater.* **2019**, *31*, No. 1901183.
(43) Brakkee, R.; Williams, R. M. Minimizing Defect States in Lead Halide Perovskite Solar Cell Materials. *Appl. Sci.* **2020**, *10*, 3061.
(44) Meggiolaro, D.; De Angelis, F. First-principles Modeling of Defects in Lead Halide Perovskites: Best Practices and Open Issues. *ACS Energy Lett.* **2018**, *3*, 2206−2222.
(45) Nenon, D. P.; Pressler, K.; Kang, J.; Koscher, B. A.; Olshansky, J. H.; Osowiecki, W. T.; Koc, M. A.; Wang, L. W.; Alivisatos, A. P. Design Principles for Trap-Free $CsPbX_3$ Nanocrystals: Enumerating and Eliminating Surface Halide Vacancies with Softer Lewis Bases. *J. Am. Chem. Soc.* **2018**, *140*, 17760−17772.
(46) Kim, J.; Cho, S.; Dinic, F.; Choi, J.; Choi, C.; Jeong, S. M.; Lee, J.-S.; Voznyy, O.; Ko, M. J.; Kim, Y. Hydrophobic Stabilizer-anchored Fully Inorganic Perovskite Quantum Dots Enhance Moisture Resistance and Photovoltaic Performance. *Nano Energy* **2020**, *75*, No. 104985.
(47) Rambabu, D.; Bhattacharyya, S.; Singh, T.; M, L. C.; Maji, T. K. Stabilization of $MAPbBr_3$ Perovskite Quantum Dots on Perovskite MOFs by a One-Step Mechanochemical Synthesis. *Inorg. Chem.* **2020**, *59*, 1436−1443.
(48) Uyanga, K. A.; Ezike, S. C.; Onyedika, A. T.; Kareem, A. B.; Chiroma, T. M. Effect of Acetic Acid Concentration on Optical Properties of Lead Acetate Based Methylammonium Lead Iodide Perovskite Thin Film. *Opt. Mater.* **2020**, *109*, No. 110456.
(49) Wang, Y.; Yuan, J.; Zhang, X.; Ling, X.; Larson, B. W.; Zhao, Q.; Yang, Y.; Shi, Y.; Luther, J. M.; Ma, W. Surface Ligand Management Aided by a Secondary Amine Enables Increased Synthesis Yield of $CsPbI_3$ Perovskite Quantum Dots and High Photovoltaic Performance. *Adv. Mater.* **2020**, *32*, No. 2000449.
(50) Nguyen, T. P.; Ozturk, A.; Park, J.; Sohn, W.; Lee, T. H.; Jang, H. W.; Kim, S. Y. Facile Synthesis of $CsPbBr_3$/PbSe Composite Clusters. *Sci. Technol. Adv. Mater.* **2018**, *19*, 10−17.
(51) Peng, L.; Geng, J.; Ai, L.; Zhang, Y.; Xie, R.; Yang, W. Room Temperature Synthesis of Ultra-small, Near-unity Single-sized Lead Halide Perovskite Quantum Dots with Wide Color Emission Tunability, High Color Purity and High Brightness. *Nanotechnology* **2016**, *27*, No. 335604.
(52) Xu, Y. B.; Zhang, Q.; Lv, L. F.; Han, W. Q.; Wu, G. H.; Yang, D.; Dong, A. G. Synthesis of Ultrasmall $CsPbBr_3$ Nanoclusters and Their Transformation to Highly Deep-blue-emitting Nanoribbons at Room Temperature. *Nanoscale* **2017**, *9*, 17248−17253.
(53) Huang, H.; Raith, J.; Kershaw, S. V.; Kalytchuk, S.; Tomanec, O.; Jing, L.; Susha, A. S.; Zboril, R.; Rogach, A. L. Growth Mechanism of Strongly Emitting $CH_3NH_3PbBr_3$ Perovskite Nanocrystals With a Tunable Bandgap. *Nat. Commun.* **2017**, *8*, No. 996.
(54) Tong, Y.; Ehrat, F.; Vanderlinden, W.; Cardenas-Daw, C.; Stolarczyk, J. K.; Polavarapu, L.; Urban, A. S. Dilution-Induced Formation of Hybrid Perovskite Nanoplatelets. *ACS Nano* **2016**, *10*, 10936−10944.
(55) Jin, C.; Feng, M.; Zhong, J.; Sun, X.; Wu, J.; Li, Q.; Gu, J.; Liu, S. Insights Into Mechanism of Size-controlled Synthesis of $CH_3NH_3PbBr_3$ Perovskite Quantum Dots and Large Nanoparticles With Tunable Optical Properties. *Org. Electron.* **2020**, *82*, No. 105712.
(56) McKenna, B.; Shivkumar, A.; Charles, B.; Evans, R. C. Synthetic Factors Affecting the Stability of Methylammonium Lead Halide Perovskite Nanocrystals. *Nanoscale* **2020**, *12*, 11694−11702.
(57) Peng, L.; Dutta, A.; Xie, R.; Yang, W.; Pradhan, N. Dot−Wire−Platelet−Cube: Step Growth and Structural Transformations in CsPbBr3 Perovskite Nanocrystals. *ACS Energy Lett.* **2018**, *3*, 2014−2020.
(58) Liu, B.; Li, J.; Duan, G.; Ji, M.; Lu, Y.; Yan, T.; Cao, B.; Liu, Z. Study on Organic-inorganic Hybrid Perovskite Nanocrystals with Regular Morphologies and Their Effect on Photoluminescence Properties. *Opt. Express* **2020**, *28*, 10714−10724.
(59) Xue, J.; Wang, R.; Yang, Y. The surface of halide perovskites from nano to bulk. *Nat. Rev. Mater.* **2020**, 809−827.

https://dx.doi.org/10.1021/acsanm.0c02894
ACS Appl. Nano Mater. 2020, 3, 12379−12387

(60) Vickers, E. T.; Enlow, E. E.; Delmas, W. G.; DiBenedetto, A. C.; Chowdhury, A. H.; Bahrami, B.; Dreskin, B. W.; Graham, T. A.; Hernandez, I. N.; Carter, S. A.; Ghosh, S.; Qiao, Q.; Zhang, J. Z. Enhancing Charge Carrier Delocalization in Perovskite Quantum Dot Solids with Energetically Aligned Conjugated Capping Ligands. *ACS Energy Lett.* **2020**, *5*, 817−825.
(61) Xu, K.; Vickers, E. T.; Rao, L.; Lindley, S. A.; Allen, A. C.; Luo, B.; Li, X.; Zhang, J. Z. Synergistic Surface Passivation of $CH_3NH_3PbBr_3$ Perovskite Quantum Dots with Phosphonic Acid and (3-Aminopropyl)triethoxysilane. *Chem. - Eur. J.* **2019**, *25*, 5014−5021.
(62) Vickers, E. T.; Graham, T. A.; Chowdhury, A. H.; Bahrami, B.; Dreskin, B. W.; Lindley, S.; Naghadeh, S. B.; Qiao, Q.; Zhang, J. Z. Improving Charge Carrier Delocalization in Perovskite Quantum Dots by Surface Passivation with Conductive Aromatic Ligands. *ACS Energy Lett.* **2018**, *3*, 2931−2939.
(63) Vickers, E. T.; Chen, Z. Y.; Cherrette, V.; Smart, T.; Zhang, P.; Ping, Y.; Zhang, J. Z. Interplay between Perovskite Magic Sized Clusters and Amino Lead Halide Molecular Clusters. *Research* **2020**, In press.
(64) Luo, B.; Naghadeh, S. B.; Allen, A. L.; Li, X.; Zhang, J. Z. Peptide-Passivated Lead Halide Perovskite Nanocrystals Based on Synergistic Effect between Amino and Carboxylic Functional Groups. *Adv. Funct. Mater.* **2017**, *27*, No. 1604018.
(65) Suh, Y. H.; Kim, T.; Choi, J. W.; Lee, C. L.; Park, J. High-Performance $CsPbX_3$ Perovskite Quantum-Dot Light-Emitting Devices via Solid-State Ligand Exchange. *ACS Appl. Nano Mater.* **2018**, *1*, 488−496.
(66) Kim, Y.; Yassitepe, E.; Voznyy, O.; Comin, R.; Walters, G.; Gong, X.; Kanjanaboos, P.; Nogueira, A. F.; Sargent, E. H. Efficient Luminescence from Perovskite Quantum Dot Solids. *ACS Appl. Mater. Interfaces* **2015**, *7*, 25007−25013.
(67) Spildo, K.; Blokhus, A. M.; Andersson, A. Surface and Interfacial Properties of Octanoic Acid-Octylamine Mixtures in Isooctane-Water Systems: Influence of Acid: Amine Molar Ratio and Aqueous Phase pH. *J. Colloid Interface Sci.* **2001**, *243*, 483−490.
(68) Luo, B.; Naghadeh, S. B.; Zhang, J. Z. Lead Halide Perovskite Nanocrystals: Stability, Surface Passivation, and Structural Control. *ChemNanoMat* **2017**, *3*, 456−465.
(69) Zhang, J. Z. A "Cocktail" Approach to Effective Surface Passivation of Multiple Surface Defects of Metal Halide Perovskites Using a Combination of Ligands. *J. Phys. Chem. Lett.* **2019**, 5055−5063.

https://dx.doi.org/10.1021/acsanm.0c02894
ACS Appl. Nano Mater. 2020, 3, 12379−12387